GIS-Based Integration of Landsat-Derived Indicators for Environmental Assessment of the Shurtan Gas Field, Uzbekistan

Fazilov, A.,[1] Fazilova, D.,[2,3*] Magdiev, Kh.,[2,4] and Khalimov, B.[2]
[1]Information Technology in Construction Department, Tashkent University of Architecture and Civil Engineering, Republic of Uzbekistan, E-mail: faz_ali@mail.ru
[2]Space Geodesy and Geodynamics Laboratory, Ulugh Beg Astronomical Institute of Uzbekistan Academy of Sciences, Republic of Uzbekistan, E-mail: dil_faz@yahoo.com*
[3]*Mine Surveying and Geodesy Department, Tashkent State Technical University Named after Islam Karimov, Republic of Uzbekistan*
[4]Project coordination office, Ministry of Economy and Finance of the Republic Uzbekistan, Republic of Uzbekistan, E-mail: hasan.magdiev@gmail.com
**Corresponding Author*

DOI: https://doi.org/10.52939/ijg.v22i8.5141

Abstract
Arid hydrocarbon landscapes are challenging to assess because surface temperatures, sparse vegetation, and exposed soils may reflect natural dryland conditions and local surface modification. This study applied a reproducible, sensitivity-tested Landsat-based framework to characterize surface environmental conditions within and around the Shurtan gas field, Uzbekistan, during 2014–2025. Annual June–September composites were generated from 484 Landsat 8 and Landsat 9 Collection 2 Level-2 scenes in Google Earth Engine (GEE). Land-surface temperature (LST), the Modified Soil Adjusted Vegetation Index (MSAVI), and the Bare Soil Index (BSI) were normalized and integrated into the Surface Environmental Condition Index (SECI), a relative composite in which higher values indicate warmer surfaces, lower soil-adjusted vegetation signal, and stronger bare-surface expression. Indicator weights were derived using the CRiteria Importance Through Intercriteria Correlation (CRITIC) method. Patterns were evaluated through zonal statistics, land-cover stratification, high-SECI frequency and persistence, the Mann–Kendall trend test, Sen slope estimation, and sensitivity analyses of normalization, spatial extent, and indicator selection. CRITIC assigned weights of 0.428 to LST, 0.324 to inverse MSAVI, and 0.248 to BSI. Mean SECI was higher in the analytical field core (0.863) than outside the field core within the 10-km analysis extent (0.698). Persistent high-SECI conditions occupied 19.8% of the field core, compared with 10.2% outside it. High SECI values occurred mainly in dryland natural vegetation and bare or sparse surfaces, underscoring land-cover context. Significant increasing SECI trends ($p < 0.05$) covered 51.8% of the field core and 44.0% of the 10-km analysis extent, whereas significant decreasing trends occupied only a limited area. Sensitivity tests showed stability across alternative normalization schemes and spatial extents, while LST was the most influential component. The framework provides a spatially explicit baseline for monitoring changing surface environmental conditions in arid gas-field landscapes and for directing future studies that integrate operational, climatic, and field observations.

Keywords: Bare Soil Index, CRITIC Method, Land-Surface Temperature, Modified Soil Adjusted Vegetation Index, Surface Environmental Condition Index

1. Introduction

1.1 Background and Motivation

Drylands cover about 41% of the global land surface and are characterized by soil-moisture limitation caused by low precipitation and high evaporative demand [1]. These conditions produce naturally sparse vegetation, extensive exposed mineral surfaces, and high summer land-surface temperatures, which are also the same satellite-observed properties often used to indicate land degradation or surface disturbance [2] and [3]. Previous studies of dryland degradation assessment have shown that vegetation-index patterns and trends are strongly affected by rainfall variability, land use, grazing, and other background environmental controls, making it difficult to infer degradation or human impact from a single spectral or thermal indicator alone [4] and [5]. Therefore, a defensible satellite-based assessment in arid regions should first establish the observable surface condition, its spatial distribution, temporal persistence, and trend behavior before assigning causal explanations to the mapped patterns.

Oil and gas fields in arid and semi-arid landscapes represent a specific case of dryland surface monitoring, where natural aridity may coincide with infrastructure-related land-cover modification. Previous studies in comparable regions have reported vegetation-production losses [6], shrubland and grassland reduction associated with production intensity [7], replacement and fragmentation of native vegetation by well pads and roads [8], increased potential for dust emission from disturbed surfaces [9], and vegetation and habitat impact near gas infrastructure in semi-arid Uzbekistan [10]. These findings indicate that vegetation condition, exposed soil, and land-surface temperature are relevant variables for satellite-based screening of surface conditions around hydrocarbon infrastructure, while causal interpretation requires additional explanatory data on infrastructure, production, land use, and local environmental factors. Remote sensing has also been applied to environmental impact assessment in other extractive landscapes, including the monitoring of mining-related surface changes and associated environmental conditions [11].

Central Asia is predominantly arid or semi-arid and is characterized by strong spatial contrasts between deserts, rangelands, irrigated land, settlements, and industrial surfaces. Regional analysis of Normalized Difference Vegetation Index (NDVI) dynamics for 2001-2020 reported a low mean vegetation signal and substantial geographic heterogeneity, with vegetation changes related to both climatic and human factors [12]. This makes a single vegetation threshold unsuitable for comparing different surface types across Central Asian drylands. The Shurtan gas field belongs to the southeastern Bukhara–Khiva region of the Amu Darya petroleum basin [13]. Intensive deep drilling and geophysical surveys have been conducted in the region since the 1950s [14]. The field includes gas and gas-condensate accumulations, and approximately 200 boreholes have been reported in this area; recent production-related observations indicate that operational activity is concentrated mainly in the central and eastern to southeastern parts of the field [14]. However, to the best of our knowledge, no previous study has provided a Landsat time-series assessment specifically for the Shurtan gas field that jointly examines land-surface temperature, soil-adjusted vegetation signal, and bare-surface expression. Such an assessment is needed because land-monitoring guidance emphasizes the interpretation of land-cover and productivity-related evidence against a baseline and within land-cover context [15], which is particularly important in heterogeneous arid industrial landscapes.

1.2 Review of Related Approaches

Several alternative approaches could be used for land-condition assessment, but their suitability depends on the research objective and available data. Principal Component Analysis (PCA)-based Remote Sensing Ecological Index (RSEI) models reduce subjective weighting by combining greenness, wetness, dryness, and heat into a principal ecological-quality component [16] and [17]. However, conventional RSEI may suffer from temporal comparability problems because PCA loadings and component signs can vary between image dates; this limitation has motivated the development of time-series RSEI modifications specifically designed to improve stability through time [18] and [19]. Geographic Information System-based Multi-Criteria Decision Analysis (GIS-MCDA), including Weighted Linear Combination (WLC), AHP, and fuzzy-AHP approaches, is widely used to integrate heterogeneous environmental indicators and generate spatially explicit composite assessments [20] [21] and [22]. However, AHP and fuzzy-AHP approaches rely on expert pairwise comparisons and consistency assessment [23] and therefore require a defensible expert-weighting framework and locally validated auxiliary data for environmental applications [21] and [22]. Information-entropy principles provide a theoretical basis for entropy-based weighting [24], while data-driven weighting approaches have been considered within multiple-criteria decision-making frameworks [25]. The CRITIC (CRiteria Importance Through Intercriteria Correlation) method derives objective weights from indicator contrast and inter-indicator correlation, thereby reducing dependence on expert judgment [26]. Machine-learning methods such as Random Forest (RF) and Extreme Gradient Boosting (XGBoost) can classify desertification or degradation patterns from multiple spectral indices, but they require reliable training and validation samples [27]. Regression and fixed-effects panel models are more suitable for causal attribution because they incorporate explanatory variables such as wells, production volume, infrastructure, land cover, and climate, as demonstrated for the Permian Basin [7]. Small Baseline Subset Interferometric Synthetic Aperture Radar (SBAS-InSAR) and multi-temporal InSAR are effective for mapping hydrocarbon-related ground deformation, but they measure displacement rather than optical–thermal surface conditions [28] and [29].

1.3 Research Gap, Study Rationale, and Objectives

For the Shurtan gas-field area, the available data situation differs from the requirements of causal, expert-driven, supervised classification, or deformation-only approaches. Spatially explicit time series of infrastructure expansion, production intensity, field-validated degradation classes, soil properties, and surface-moisture observations are not available at a resolution and temporal coverage comparable to Landsat. At the same time, Landsat provides a consistent multi-year record of land-surface temperature, vegetation response, and bare-surface expression, which are widely used as observable indicators in dryland and oil/gas landscape monitoring [2] [7] and [10]. A suitable method for this study must therefore be reproducible, based on consistently available satellite indicators, avoid subjective expert weights, account for correlation among indicators, and allow explicit sensitivity testing. Among objective weighting methods, CRITIC is appropriate for this purpose because it accounts for both indicator contrast and inter-indicator correlation, thereby reducing redundancy among statistically related indicators [26]. Therefore, this study uses the long Landsat record and an objectively weighted composite-index framework to characterize the spatial distribution, temporal persistence, trends, and methodological robustness of observable surface environmental conditions within and around the Shurtan gas field. The resulting SECI is defined as a relative composite descriptor derived from land-surface temperature, inverse soil-adjusted vegetation signal, and bare-surface expression. Higher SECI values indicate a combination of relatively warmer, less vegetated, and more exposed surfaces within the selected analysis domain and period. SECI is not interpreted as a direct measure of environmental degradation, ecological stress, or gas-production impact. The scientific contribution of this study lies in applying a reproducible and sensitivity-tested Landsat-based assessment framework to an arid gas-field landscape with limited auxiliary data. The framework further evaluates the persistence, trend behavior, and methodological sensitivity of the mapped surface-condition patterns.

The aim of this study is to assess the spatial and temporal variability of surface environmental conditions within and around the Shurtan gas field using Landsat-derived indicators and an objective composite-index framework. The specific objectives are: (i) to construct annual warm-season Landsat composites for 2014-2025; (ii) to derive surface-temperature, vegetation, and bare-soil indicators suitable for arid environments; (iii) to integrate these indicators into the Surface Environmental Condition Index (SECI) using objective weighting; (iv) to compare SECI patterns between the analytical field core and its surrounding area; and (v) to evaluate hotspot persistence, trend significance, and sensitivity to normalization, indicator selection, and analysis extent.

2. Methodology

2.1 Study Area

The study area is centered on the Shurtan gas field in southern Uzbekistan, within the southeastern Bukhara–Khiva region of the Amudarya Basin (Figure 1). The Shurtan field is located within the Beshkent depression of the southeastern Amu Darya Basin. Regional petroleum-system studies identify Upper Jurassic carbonate successions as important hydrocarbon-bearing units within the basin [30]. Lower Cretaceous siliciclastic reservoirs and associated stratigraphic traps have also been documented in the broader Kopeh Dagh–Amu Darya Basin [31]. This geological setting is described only as regional background information. Geological units were not included in the SECI workflow because the index was designed to characterize observable surface environmental conditions derived directly from multi-year Landsat indicators, namely land-surface temperature, soil-adjusted vegetation response, and bare-surface expression. In addition, generalized surface geological classes are static over the 2014–2025 observation period and may not adequately represent subsurface reservoir structure, production intensity, or local surface disturbance. Therefore, geology was not used as an index component, weighting criterion, or classification variable.

The area is characterized by an arid lowland environment, sparse vegetation, high summer temperatures, exposed surfaces, irrigated and non-irrigated land-cover mosaics, and locally developed settlement and infrastructure corridors. These background conditions are important because low vegetation cover, high bare-surface expression, and elevated land-surface temperature may occur naturally in drylands and should not be interpreted individually as evidence of local disturbance.

For this reason, the spatial framework was designed to compare the field-centered surface pattern with the surrounding arid context rather than to infer causality from the field boundary alone. The Shurtan field has been investigated and developed over several decades; previous geodetic work reports long-term drilling and geophysical exploration,

ISSN: 1686-6576 (Printed) | ISSN 2673-0014 (Online) | © Geoinformatics International

approximately 200 boreholes, and operational activity concentrated mainly in the central and eastern parts of the study area [14]. These data provide useful regional and operational context, but they were not used to construct the SECI, define the analytical boundary, or assign index weights.

The study design distinguishes between a core field area (FIELD) and a broader region of interest (ROI) in order to analyze both field-centered surface conditions and the surrounding environmental background (Figure 1). In the analysis, the field area is represented by an analytical rectangular field core bounded by 65.80°-66.20°E and 38.40°-38.60°N. This polygon is used only as a reproducible analytical unit for zonal comparison and should not be interpreted as an official license, administrative, or production boundary. The main ROI was generated as an exact 10-km rectangular buffer around the analytical field core. This distance was used as a pragmatic baseline analysis extent, not as an assumed impact radius or production boundary. Comparable kilometre-scale analysis buffers have been used in remote-sensing studies of mining and energy-infrastructure landscapes [32] and [33]. The 10-km ROI was used for SECI normalization, mapping, and zonal statistics. To test sensitivity to spatial extent, additional ROI buffers of 5, 15, 20, and 25 km were used; these alternative extents were not treated as separate study zones and are not shown in Figure 1.

Land-cover information was included to characterize the surface context of the study area and to support interpretation of the Landsat-derived indicators. ESA WorldCover 2021 was used because it provides a global land-cover product at 10 m spatial resolution based on Sentinel-1 and Sentinel-2 data and includes 11 land-cover classes [34]. For this study, the original WorldCover classes were regrouped into broader categories for cartographic interpretation: natural vegetation, cropland, built-up areas, bare or sparse surfaces, water/wetland, and other classes. As shown in Figure 1, the analytical field core and surrounding ROI include a heterogeneous land-cover mosaic, with extensive open or sparsely covered surfaces, cropland areas, built-up patches and infrastructure corridors, and limited water or wetland features. This land-cover context was used for interpretation, masking of water/wetland pixels where necessary, and stratified descriptive statistics. It was not included as a weighted SECI component because SECI was constructed exclusively from Landsat-derived indicators: land-surface temperature, soil-adjusted vegetation response, and bare-surface expression. Geological setting was described only as regional background information and was not used as an input layer in the SECI workflow.

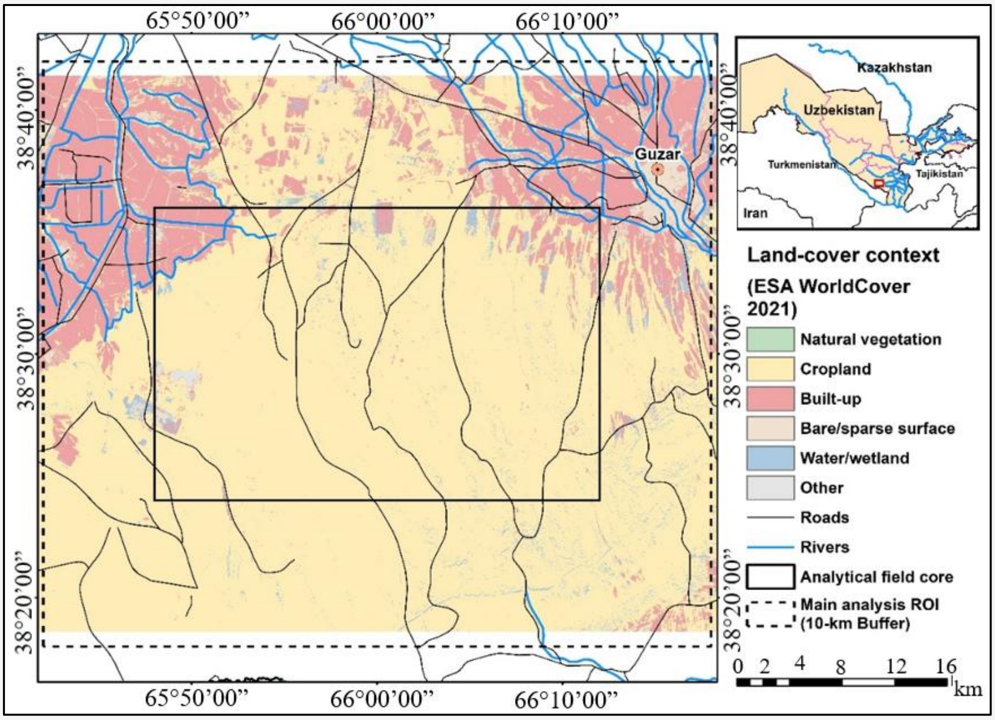

Figure 1: Location and spatial framework of the Shurtan study area, Uzbekistan

ISSN: 1686-6576 (Printed) | ISSN 2673-0014 (Online) | © Geoinformatics International

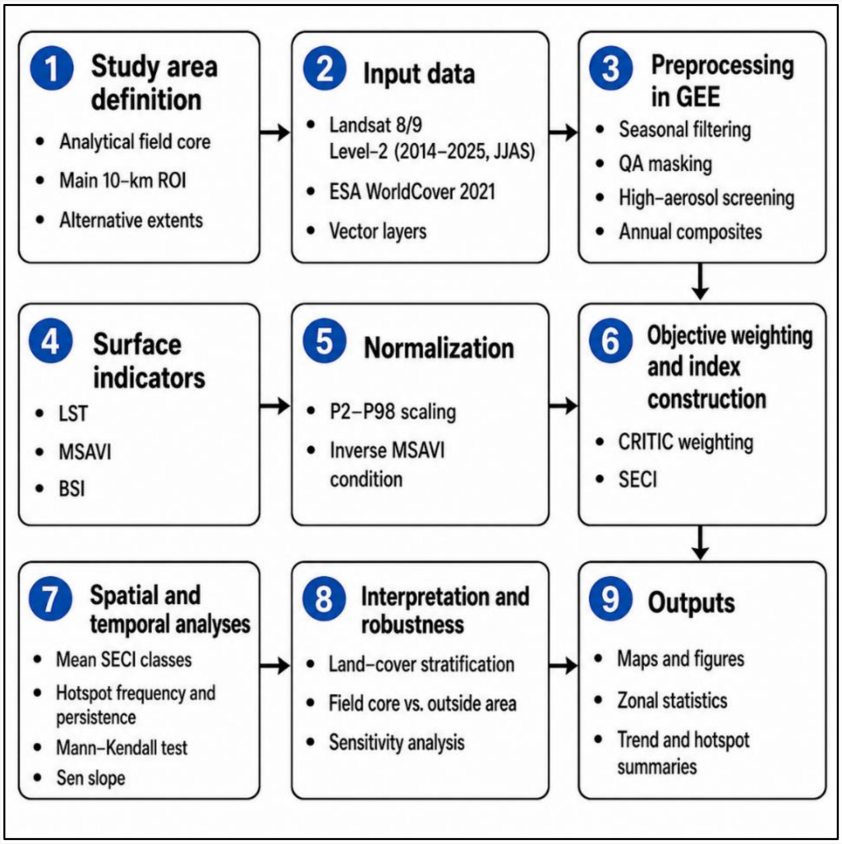

Figure 2: Schematic workflow of SECI construction and analysis

2.2 Landsat Data Processing and SECI Construction

The methodological workflow is summarized in Figure 2. The analysis used Landsat 8 and Landsat 9 Collection 2 Level-2 surface reflectance and surface temperature products for 2014–2025, ESA WorldCover 2021 land-cover data, and vector layers representing the analytical field core, ROI, roads, rivers, and settlement locations. Landsat Collection 2 Level-2 products provide atmospherically corrected surface reflectance and surface temperature products [35]. ESA WorldCover 2021 was used only to characterize land-cover context, support water/wetland masking, and provide stratified descriptive statistics; it was not included as a weighted SECI component. All satellite raster processing was performed in the GEE cloud environment using JavaScript in the Code Editor [36], while final cartographic layouts were prepared in ArcGIS.

After seasonal and spatial filtering, 484 Landsat scenes were retained for the 2014–2025 JJAS analysis, including 360 Landsat 8 scenes and 124 Landsat 9 scenes. Annual scene availability ranged from 28 to 62 scenes per year: 28–32 scenes per year during 2014–2021, when only Landsat 8 was available in the dataset, and 60–62 scenes per year during 2022–2025 after the inclusion of Landsat 9. The monthly distribution was balanced, with 120 scenes in June, 120 in July, 124 in August, and 120 in September. Scene-level cloud cover was generally low for most images, with a mean of 4.85% and a median of 0.13%, although the maximum scene-level cloud cover reached 72.37%. Cloudy, shadowed, cirrus-affected, saturated, and high-aerosol pixels were removed during pixel-level preprocessing. The study area was covered by four WRS-2 footprints: path/row 155/33, 155/34, 156/33, and 156/34.

Annual warm-season composites were generated for June–September (JJAS) to ensure interannual comparability under a consistent warm- and dry-season observation window. This warm-season design does not characterize spring or cool-season vegetation dynamics; therefore, the resulting SECI patterns and trends are specific to JJAS conditions and should not be generalized to the full annual cycle. Clouds, cloud shadows, cirrus, snow, fill pixels, radiometrically saturated observations, and high-aerosol observations were masked using QA_PIXEL, QA_RADSAT, and SR_QA_AERO SOL according to the Landsat Collection 2 Level-2 quality-assurance definitions [35]. Although high-aerosol observations were removed, residual aerosol effects may remain in dusty arid conditions and should be considered when interpreting individual

ISSN: 1686-6576 (Printed) | ISSN 2673-0014 (Online) | © Geoinformatics International

annual composites. For each year, LST, MSAVI, and BSI were composited using the pixel-wise median of all valid JJAS observations. Pixels with fewer than three valid observations in a given year were masked, and pixels with valid annual values in fewer than 10 years during 2014–2025 were excluded from multi-year mean and trend analyses. Surface reflectance and temperature bands were scaled using the official USGS Collection 2 scale factors and offsets [35] and [37].

Three Landsat-derived indicators were selected: land-surface temperature (LST), Modified Soil Adjusted Vegetation Index (MSAVI), and Bare Soil Index (BSI). LST represents thermal surface response and is widely used in remote-sensing ecological assessments, including RSEI-type approaches [16] and [17]. Landsat-based studies have also demonstrated the importance of interpreting LST together with land-cover and vegetation patterns when assessing environmental dynamics [38]. MSAVI was used instead of NDVI because sparse vegetation and strong soil-background influence are characteristic of the study area, and MSAVI was specifically designed to reduce soil effects on the vegetation signal [39]. SAVI and MSAVI primarily characterize vegetation response rather than bare-surface expression. BSI was therefore retained as a complementary indicator of exposed or bare surfaces because it can be calculated consistently from Landsat reflectance data [40]. NDBI was not selected because it is primarily intended to enhance built-up surfaces and may not clearly distinguish infrastructure from naturally exposed soil in an arid landscape, whereas spectral mixture analysis would require robust endmember definition and validation across years. Accordingly, BSI is used here as a reproducible descriptor of exposed-surface expression rather than as a universally optimal or direct measure of soil degradation; it may also vary with natural substrate, surface moisture, and land-cover conditions. These indicators were treated as complementary descriptors of observable surface conditions, not as individual evidence of degradation or gas-field impact.

Before calculating spectral indices, Landsat surface reflectance bands were scaled according to the Collection 2 Level-2 specifications. Equation 1 was used to convert the original digital numbers into scaled surface reflectance values:

$$P_{\lambda} = 0.0000275 DN_{\lambda} - 0.2$$

Equation 1

Where:

ρ_{λ} = scaled surface reflectance for spectral band λ

DN_{λ} = original digital number of the corresponding Landsat Level-2 surface reflectance band.

LST (°C) was derived from the Landsat Collection 2 Level-2 surface temperature band (ST_B10) using the official scale factor and offset provided in the Landsat 8–9 Collection 2 Level-2 Science Product Guide [35]. Equation 2 was used for LST calculation:

$$LST = (0.00341802 \times ST\_B10) + 149 - 273.15$$

Equation 2

Where:

LST = Land-surface temperature (°C)

ST_B10 = Digital number of the Landsat thermal surface temperature band

MSAVI was calculated to represent vegetation signal while reducing the influence of bright soil background. Equation 3 was used to calculate MSAVI:

$$MSAVI = \frac{1}{2}\left(\rho_{NIR} + 1 + \sqrt{\left(2\rho_{NIR}+1\right)^2 - 8\left(\rho_{NIR} - \rho_{RED}\right)}\right)$$

Equation 3

Where:

ρ_{NIR} = surface reflectance in the near-infrared band

ρ_{Red} = surface reflectance in the red band

Higher MSAVI values indicate a stronger vegetation signal, whereas lower values indicate sparse or absent vegetation cover. BSI was calculated to characterize the relative expression of exposed or bare surfaces. Equation 4 was used to calculate BSI:

$$BSI = \frac{\left(\rho_{SWIR1} + \rho_{RED}\right) - \left(\rho_{NIR} + \rho_{BLUE}\right)}{\left(\rho_{SWIR1} + \rho_{RED}\right) + \left(\rho_{NIR} + \rho_{BLUE}\right)}$$

Equation 4

Where:

ρ_{SWIR1}, ρ_{RED}, ρNIR, and $\rho Blue$ = surface reflectance values in the shortwave infrared 1, red, near-infrared, and blue bands, respectively.

For visual interpretation, the mean LST, MSAVI, and BSI component maps were displayed in ArcGIS using a Percent Clip stretch with 2% clipping at both lower and upper tails. This procedure affects only cartographic visualization and does not modify the raster values used in statistical analysis or SECI calculation. Quantitative analyses were performed using the original raster values.

Since the three indicators have different physical units and value ranges, they were normalized to a common 0–1 scale before integration. A multi-year reference image was first generated as the pixel-wise median of the annual LST, MSAVI, and BSI composites for 2014–2025, retaining only pixels with valid annual values in at least 10 years. To reduce the influence of extreme values, robust percentile-based min–max normalization was applied using the 2nd and 98th percentiles calculated from the reference image within the main 10-km ROI at a 120-m statistics scale. The 120-m scale was used only for regional statistical calculations as a pragmatic compromise between preserving the broad spatial patterns represented by the original 30-m Landsat products and reducing computational load and spatial oversampling across the large study area. All final raster products were generated and exported at 30-m spatial resolution. The use of the 120-m statistical scale does not imply removal of spatial autocorrelation or statistical independence among neighbouring observations. Values below P2 and above P98 were clipped to 0 and 1, respectively. The P2–P98 range was used as the baseline normalization scheme and was evaluated against P1–P99 and P5–P95 alternatives in the sensitivity analysis. The resulting normalization bounds were then applied unchanged to all annual indicator images. Equation 5 was used for percentile-based normalization:

$$X_{norm} = \frac{X - P2_x}{P98_x - P2_x}$$

Equation 5

Where:

X_{norm} = normalized value of indicator X

X = original indicator value

$P2_X$ = 2nd percentile of indicator X

$P98_X$ = 98th percentile of indicator X

Values below $P2_X$ were set to 0, and values above $P98_X$ were set to 1. Therefore, SECI values should be interpreted as relative surface environmental conditions within the selected analysis domain and period.

For LST and BSI, higher normalized values indicate warmer and more exposed surface conditions. For MSAVI, the direction was inverted so that lower vegetation signal contributed to higher SECI values. Equation 6 was used to define the condition-oriented components:

$$LST_{cond} = LST_{norm}$$
$$BSI_{cond} = BSI_{norm}$$
$$MSAVI_{cond} = 1 - MSAVI_{norm}$$

Equation 6

Where:

LST_{cond}, BSI_{cond}, and $MSAVI_{cond}$ are condition-oriented normalized components used in SECI construction

LST_{norm}, BSI_{norm}, and $MSAVI_{norm}$ are normalized values of LST, BSI, and MSAVI, respectively.

The normalized condition components were integrated using the CRITIC objective weighting method [26]. CRITIC assigns higher weights to indicators with greater contrast and greater information conflict, while reducing the influence of redundant, strongly correlated indicators. CRITIC weights were calculated once from the normalized and condition-oriented version of the multi-year reference image. The covariance matrix and inter-indicator correlations were estimated within the main 10-km ROI at a 120-m statistics scale. The resulting weights were held fixed and applied to all annual condition-component images to maintain temporal comparability. Equation 7 was used to calculate the information content of each criterion:

$$C_j = \sigma_j \sum_{k=1}^{m} (1 - r_{jk})$$

Equation 7

Where:

C_j = CRITIC information content of criterion j

σ_j = standard deviation of criterion j

r_{jk} = correlation coefficient between criteria j and k

m = total number of criteria.

In this study, m=3, corresponding to LST_{cond}, $MSAVI_{cond}$, and BSI_{cond}

The final objective weight of each criterion was obtained by normalizing its information content. Equation 8 was used to calculate the CRITIC weights:

$$w_j = \frac{C_j}{\sum_{j=1}^{m} C_j}$$

Equation 8

Where:

w_j = final weight of criterion j

C_j = information content of criterion j

$\sum_{j=1}^{m} C_j$ = total information content of all criteria.

The SECI was then calculated as a weighted linear combination of the three normalized condition components. Equation 9 was used to calculate SECI:

$$SECI = w_{LST} LST_{cond} + w_{MSAVI} MSAVI_{cond} + w_{BSI} BSI_{cond}$$

Equation 9

Where:

$SECI$ = Surface Environmental Condition Index

w_{LST}, w_{MSAVI}, and w_{BSI} = CRITIC-derived weights

Higher SECI values indicate relatively warmer surfaces, lower soil-adjusted vegetation signal, and

ISSN: 1686-6576 (Printed) | ISSN 2673-0014 (Online) | © Geoinformatics International

stronger bare-surface expression within the selected analysis domain. SECI is therefore interpreted as a relative composite descriptor of observable surface environmental conditions within the selected analysis domain and period. Identification of the processes controlling these conditions requires complementary environmental and operational data.

For cartographic interpretation, mean SECI values were classified using percentile-based classes rather than equal intervals. The 20th, 40th, 60th, and 80th percentiles were used as class thresholds. This approach was selected because SECI is a relative index and because equal-interval classes may be unsuitable for skewed arid-land distributions. The P20, P40, P60, and P80 class thresholds were derived from the 2014–2025 mean SECI raster within the main 10-km ROI. The resulting P80 value was used as a fixed threshold and applied to each annual SECI image to identify high-SECI pixels. High-SECI frequency was calculated as the number of years in which each pixel exceeded this threshold. Persistent high-SECI areas were defined as pixels exceeding the fixed P80 threshold in at least 8 of 12 years, with valid SECI observations required for all 12 years. This definition identifies areas where relatively high SECI conditions recur through time.

Temporal trends in annual JJAS SECI were assessed using Sen slope [41] and the Mann–Kendall test [42] and [43]. The magnitude and direction of monotonic SECI change were estimated using Sen slope, calculated according to Equation 10:

$$\beta = median\left(\frac{SECI_j - SECI_i}{t_j - t_i}\right), \; j > i$$

Equation 10

Where:

β = Sen slope
$SECI_i$ and $SECI_j$ = annual SECI values at times t_i and t_j, respectively

Positive β values indicate increasing SECI through time, whereas negative values indicate decreasing SECI.

The Mann–Kendall statistic was used to test the significance of monotonic trends. Trends were mapped using $p < 0.05$ as the primary significance threshold, while $p < 0.01$ was additionally used as a stricter threshold for robustness assessment. Non-significant pixels were masked or shown separately in the trend-class maps. Equation 11 was used to calculate the Mann–Kendall S statistic:

$$S = \sum_{i=1}^{n-1} \sum_{j=i+1}^{n} \operatorname{sgn}\left(SECI_j - SECI_i\right)$$

Equation 11

Where:

S = Mann–Kendall test statistic
n = number of annual SECI observations
$sgn(SECI_j - SECI_i)$ = sign function

The sign function is defined as follows:

- +1 when $SECI_j - SECI_i > 0$,
- 0 when $SECI_j - SECI_i = 0$,
- −1, when $SECI_j - SECI_i < 0$.

2.3 Sensitivity and Robustness Assessment

Several sensitivity tests were performed to evaluate the robustness of the SECI results. First, sensitivity to spatial extent was assessed using analysis buffers of 5, 10, 15, 20, and 25 km. The baseline SECI model, including the normalization bounds and CRITIC weights derived from the main 10-km ROI, was kept unchanged, while summary statistics were recalculated within each alternative extent. Second, normalization sensitivity was evaluated using P1–P99, P2–P98, and P5–P95 percentile ranges. For these scenarios, the baseline CRITIC weights were held fixed, whereas normalization bounds, mean SECI products, percentile classes, and persistent high-SECI masks were recalculated. Third, leave-one-indicator-out tests were performed by excluding LST, MSAVI, or BSI in turn; CRITIC weights were recalculated using the remaining indicators. Pairwise Pearson correlations were also calculated for the raw multi-year reference indicators and for the normalized condition-oriented reference components.

Agreement with the baseline model was evaluated using the Pearson correlation coefficient, root-mean-square error, percentage class agreement, and the Jaccard similarity coefficient. Pearson correlation and root-mean-square error were calculated between continuous mean SECI rasters. Class agreement was defined as the percentage of valid pixels assigned to the same relative SECI class in the baseline and alternative models. Jaccard similarity was calculated as the area of intersection divided by the area of union of the compared persistent high-SECI masks. Zonal comparisons were performed for the analytical field core, the full 10-km ROI, and the part of the ROI located outside the field core. Standardized mean differences between the analytical field core and the part of the ROI located outside the field core were calculated as descriptive effect-size measures. Equation 12 was used to calculate the standardized mean difference:

ISSN: 1686-6576 (Printed) | ISSN 2673-0014 (Online) | © Geoinformatics International

$$SMD = \frac{\bar{X}_{field} - \bar{X}_{outside}}{\sqrt{0.5\left(S_{field}^2 + S_{outside}^2\right)}}$$

Equation 12

Where:

SMD = standardized mean difference,

$\bar{X}_{field}$ and $\bar{X}_{outside}$ = mean values of the corresponding indicator within the analytical field core and the ROI outside the field core, respectively

s_{fields} and $s_{outside}$ = standard deviations.

The resulting standardized mean differences were interpreted as descriptive effect-size measures rather than as pixel-level inferential statistics because neighbouring pixels are spatially autocorrelated and therefore cannot be considered statistically independent.

3. Results and Discussion

3.1 Landsat Data Quality and SECI Input Indicators

Annual JJAS composites provided sufficient data coverage for the 2014-2025 analysis. The area satisfying the minimum annual observation requirement exceeded 99.84% in all zones and years, and the mean number of valid observations per pixel ranged from 14.2 to 32.2. These results indicate that the annual LST, MSAVI, BSI, and SECI products were based on consistent multi-year Landsat observations. The higher observation density after 2022 reflects the combined use of Landsat 8 and Landsat 9, but all years satisfied the minimum valid-observation requirement.

The spatial patterns of the three Landsat-derived input indicators are shown in Figures 3 and 4. Maps are displayed using a 2%–98% percentile stretch for visualization; quantitative analyses were performed using the original raster values. Mean LST displayed a clear warm-season thermal contrast across the 10-km ROI (Figure 3). Higher LST values occurred mainly over open dryland surfaces, including large parts of the analytical field core, whereas lower values were associated with irrigated cropland, drainage features, settlement mosaics, and other heterogeneous surfaces. This confirms that surface temperature alone reflects a combination of arid background, land cover, and surface exposure, and should not be interpreted independently as evidence of local disturbance.

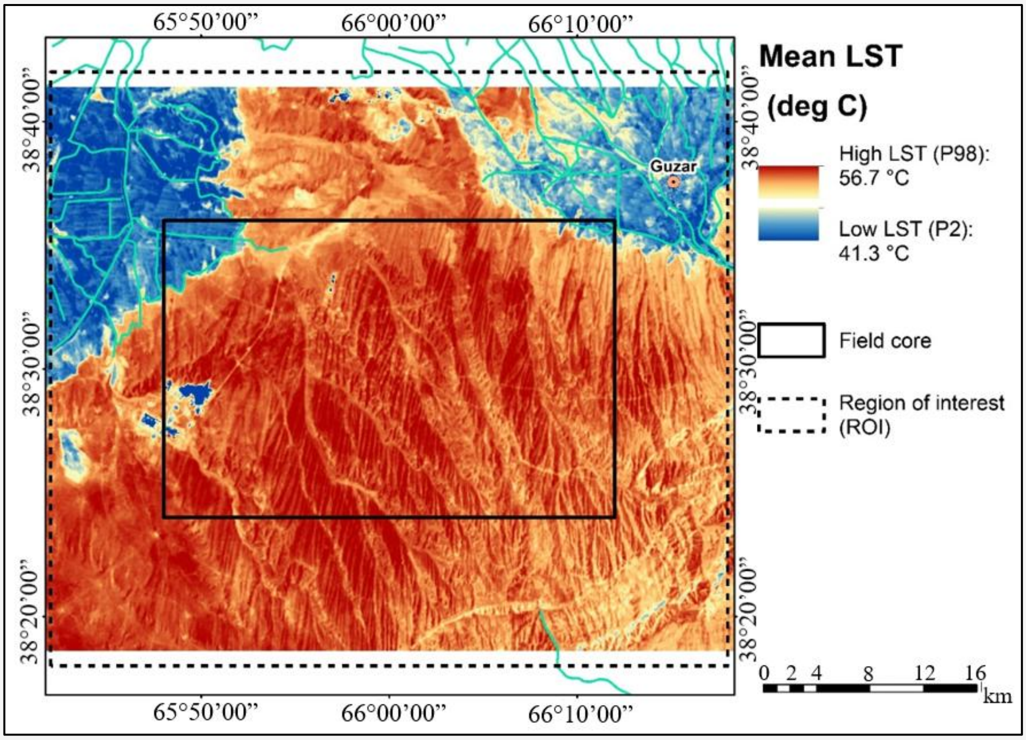

Figure 3: Mean land-surface temperature (LST) during 2014–2025

ISSN: 1686-6576 (Printed) | ISSN 2673-0014 (Online) |

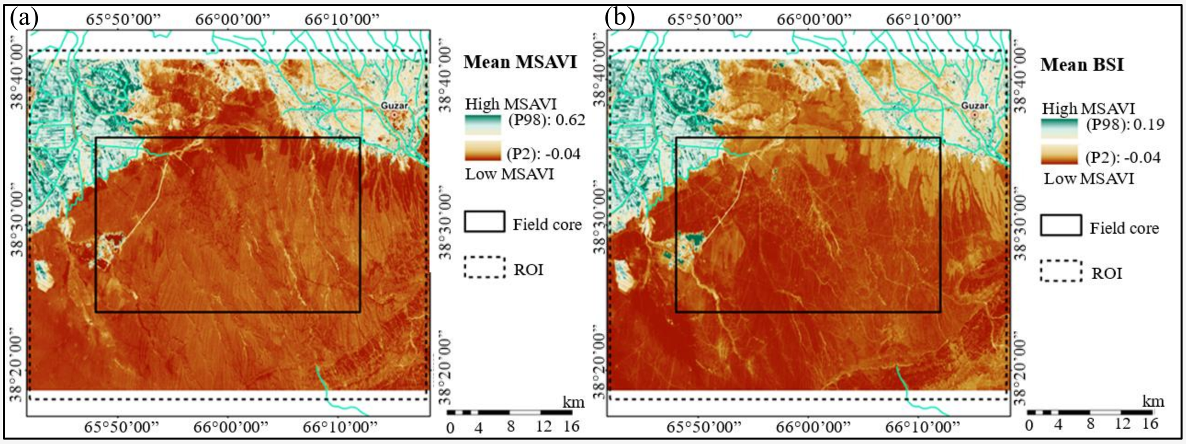

Figure 4: Mean Landsat-derived surface indicators during 2014–2025: (a) MSAVI and (b) BSI

Table 1: CRITIC weights and component correlations used in SECI construction

Metric	Component or pair	Value	Note
CRITIC weight	LST condition	0.428	Objective weight derived from contrast and inter-indicator conflict
CRITIC weight	inverse MSAVI condition	0.324	Objective weight derived from contrast and inter-indicator conflict
CRITIC weight	BSI condition	0.248	Objective weight derived from contrast and inter-indicator conflict
Raw component correlation	LST-MSAVI	0.856	Pearson r for original mean components
Raw component correlation	LST-BSI	0.945	Pearson r for original mean components
Raw component correlation	MSAVI-BSI	0.645	Pearson r for original mean components
Condition-component correlation	LST_cond-MSAVI_cond	0.984	Pearson r after orientation toward SECI condition
Condition-component correlation	LST_cond-BSI_cond	0.989	Pearson r after orientation toward SECI condition
Condition-component correlation	MSAVI_cond-BSI_cond	0.997	Pearson r after orientation toward SECI condition

MSAVI showed a contrasting spatial pattern in many parts of the ROI (Figure 4(a)). Higher MSAVI values were mainly associated with cropland and vegetated patches, whereas the field core was characterized by generally low MSAVI values, reflecting sparse vegetation and strong soil-background influence. This supports the use of MSAVI rather than NDVI in the SECI workflow because MSAVI is better suited to sparsely vegetated dryland surfaces. The BSI map showed stronger bare-surface expression across much of the field core and other open dryland areas, while lower BSI values were associated with vegetated, irrigated, or less exposed surfaces (Figure 4(b)). The spatial similarity between LST and BSI, together with the orientation of inverse MSAVI in the SECI calculation, indicates that the three components describe a common dryland surface-condition gradient: warmer, less vegetated, and more exposed surfaces tend to occur together. These indicators were therefore treated as complementary descriptors of observable surface condition, not as separate evidence of degradation or gas-field impact.

The CRITIC weighting results indicate that LST contributed the largest weight to SECI construction, followed by inverse MSAVI and BSI. The resulting weights were 0.428 for LST_cond, 0.324 for MSAVI_cond, and 0.248 for BSI_cond (Table 1). This weighting pattern is consistent with the strong thermal contrast observed in the study area and confirms that LST was the most influential component in the final SECI, while vegetation and bare-surface indicators provided additional information on surface cover and exposure. The raw component correlations and the condition-component correlations were high (Table 1), indicating that the selected indicators share a strong dryland surface gradient. This supports the use of CRITIC weighting, which accounts for inter-indicator correlation, but it also means that SECI should be interpreted as a compact descriptive composite rather than as a set of independent causal variables.

3.2 Spatial Structure of SECI and Land-Cover Context

The mean SECI map and percentile-based relative SECI levels are shown in Figure 5. SECI values ranged from 0 to 1 because the index was constructed from normalized condition-oriented indicators. Higher SECI values represent relatively warmer surfaces, lower soil-adjusted vegetation signal, and stronger bare-surface expression within the selected analysis domain. The percentile thresholds used to define relative SECI classes were 0.568 (P20), 0.850 (P40), 0.885 (P60), and 0.912 (P80). The field core had a higher mean SECI (0.863) than the area outside the field core within the 10-km ROI (0.698) and the full 10-km ROI (0.753) (Table 2). The mean difference between the field core and the area outside it was 0.165 SECI units. The corresponding standardized mean differences were 0.86 for LST, −0.63 for MSAVI, 0.67 for BSI, and 0.77 for SECI. Component statistics show the same direction of contrast: the field core was warmer by 3.23 °C, had lower MSAVI by 0.035, and had higher BSI by 0.037 relative to the area outside the field core within the 10-km ROI. Spatially, high and highest relative SECI classes were concentrated mainly in the central and southern parts of the field core and in several open dryland surfaces outside it. Lower relative SECI levels occurred mostly in the northwestern and northeastern parts of the ROI, where cropland, settlement mosaics, drainage features, and other less exposed surfaces are more common. This spatial contrast demonstrates that the field core is part of a broader dryland surface gradient rather than an isolated anomaly. The high-SECI zones were concentrated mainly in the central and southern to southeastern parts of the analytical field core. The distribution of these high-SECI zones is broadly consistent with previously reported observations at Shurtan, where operational activity was concentrated in the central and eastern parts of the study area, while the most intense GNSS-observed subsidence occurred mainly in the central part of the field [14]. This correspondence provides useful operational and geodetic context for interpreting the mapped surface patterns, although SECI, GNSS observations, and well-pressure data represent different physical characteristics. Land-cover stratification helps clarify why high SECI values cannot be interpreted only as settlement or infrastructure effects. In the field core, the highest mean SECI occurred in areas classified as natural vegetation by ESA WorldCover (0.889), followed by bare or sparse surfaces (0.832), whereas cropland and built-up areas had lower mean SECI values (0.510 and 0.571, respectively) (Table 3). In the full 10-km ROI, the same general ordering was observed: natural vegetation and bare or sparse surfaces had higher SECI values than cropland and built-up classes. In this arid setting, the WorldCover natural vegetation class mainly represents sparse natural vegetation or dryland cover, not dense vegetation.

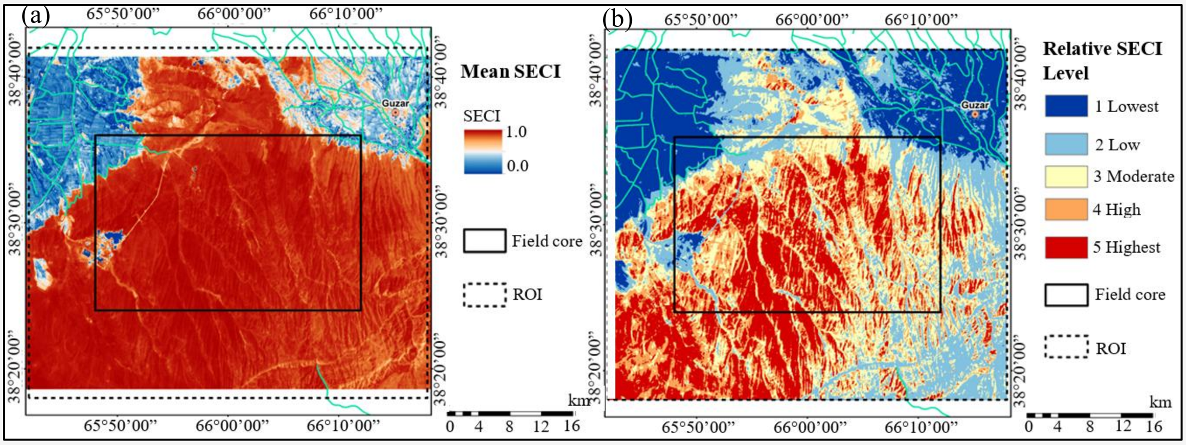

Figure 5: Mean SECI and relative SECI levels for 2014-2025: (a) mean SECI and (b) percentile-based relative SECI classes. Higher SECI values indicate relatively warmer surfaces, lower soil-adjusted vegetation signal, and stronger bare-surface expression within the selected analysis domain

Table 2: Descriptive statistics of the 2014–2025 mean Landsat-derived indicators and SECI by analysis zone

Zone	Valid area (km²)	LST mean ± SD [min–max], (°C)	MSAVI mean ± SD [min–max]	BSI mean ± SD [min–max]	SECI mean ± SD [min–max]	Persistent high-SECI area (km²)
Field core	772.0	54.19 ± 2.45 [33.47–58.78]	0.104 ± 0.032 [0.020–0.478]	0.164 ± 0.033 [-0.211–0.199]	0.863 ± 0.132 [0.006–0.986]	152.9
ROI outside field core	1,537.9	50.96 ± 4.71 [34.98–59.09]	0.138 ± 0.070 [-0.025–0.496]	0.127 ± 0.071 [-0.259–0.225]	0.698 ± 0.273 [0.000–0.969]	156.6
Full 10-km ROI	2,309.9	52.04 ± 4.37 [33.47–59.09]	0.127 ± 0.063 [-0.025–0.496]	0.139 ± 0.064 [-0.259–0.225]	0.753 ± 0.248 [0.000–0.986]	309.5

Note: "ROI outside field core" is the part of the main 10-km ROI located outside the analytical field core; it is not shown as a separate boundary in Figure 1. Values represent spatial statistics of the 2014–2025 mean indicator rasters calculated at a 120-m statistical scale. SD denotes standard deviation. Minimum and maximum values represent the observed range within each analysis zone. These statistics are descriptive and are not interpreted as independent pixel-level inferential estimates because neighbouring pixels are spatially autocorrelated.

Table 3: Land-cover-stratified SECI statistics for selected classes

Land-cover class	Field core area (km^2)	Field core mean SECI	Field core persistent high-SECI (%)	Full ROI area (km^2)	Full ROI mean SECI	Full ROI persistent high-SECI (%)
Natural vegetation	710.3	0.889	21.5%	1732.6	0.863	17.8
Cropland	47.8	0.510	0.0%	472.2	0.395	0.0
Built-up	3.2	0.571	0.5%	66.5	0.418	0.0
Bare or sparse surface	11.5	0.832	1.5%	41.8	0.778	0.8

Water/wetland and other classes are not summarized because they were masked or had no valid SECI pixels for the main analysis

Its high SECI values are therefore consistent with high LST, low soil-adjusted vegetation signal, and high bare-surface expression. Cropland and built-up classes showed lower SECI because they are often associated with irrigation, vegetation patches, mixed surfaces, or cooler land-cover mosaics. This result confirms that land cover is essential for interpretation, but it also supports the decision not to include LULC as a weighted SECI component. LULC was used to contextualize SECI values and to avoid overinterpreting high SECI as a uniquely industrial signal.

3.3 Persistence of High-SECI Conditions and SECI Trends

High-SECI frequency was assessed by counting the number of annual SECI images in which each pixel exceeded the fixed P80 threshold of 0.912, derived from the 2014–2025 mean SECI raster within the main 10-km ROI. Persistent high-SECI areas were defined as pixels exceeding this threshold in at least 8 of 12 years, with valid SECI observations required for all 12 years. Figure 6 shows that recurrent high-SECI conditions were concentrated mainly in the central and southern parts of the field core, but repeated high-SECI patches also occurred outside the field core in open dryland areas. Persistent high-SECI areas occupied 152.88 km2 of the field core, corresponding to 19.8% of its valid SECI area. In comparison, the area outside the field core within the 10-km ROI contained 156.58 km2 of persistent high-SECI areas, or 10.2% of its valid SECI area. For the full 10-km ROI, persistent high-SECI areas covered 309.46 km2, or 13.4%. Thus, the proportion of persistent high-SECI pixels was almost twice as high in the field core as in the surrounding part of the 10-km ROI, although persistent high-SECI conditions were not spatially exclusive to the field core.

This persistence analysis is important because it distinguishes recurrent high-SECI surfaces from isolated annual anomalies. However, persistence should still be interpreted as repeated occurrence of relatively warm, sparsely vegetated, and exposed surface conditions. It does not by itself identify the

ISSN: 1686-6576 (Printed) | ISSN 2673-0014 (Online) | © Geoinformatics International

cause of those conditions, which may include natural arid background, land cover, soil exposure, infrastructure, or their combination. The significant SECI trend classes for 2014-2025 are shown in Figure 7. Positive trends indicate increasing SECI, i.e., a tendency toward relatively warmer, less vegetated, and more exposed surface conditions. Negative trends indicate decreasing SECI. Non-significant pixels are shown separately and were not interpreted as trend areas. At $p < 0.05$, significant increasing SECI trends dominated over decreasing trends in all zones (Table 4). In the field core, significant increasing trends covered 399.88 km2 (51.8% of valid trend area), whereas significant decreasing trends covered only 3.59 km2 (0.46%). The area outside the field core within the 10-km ROI also showed more increasing than decreasing trends: 615.50 km2 (40.0%) increased significantly, while 18.92 km2 (1.23%) decreased significantly.

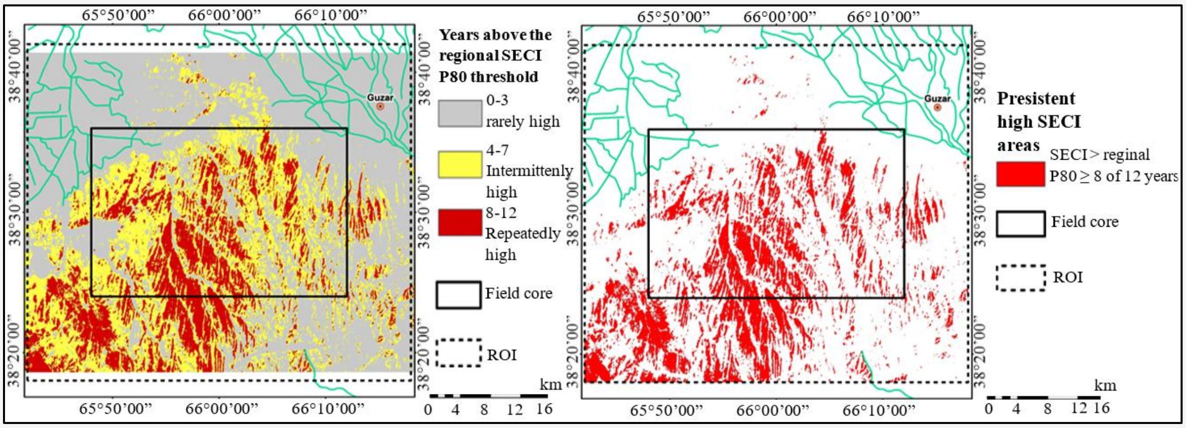

Figure 6: Frequency and persistence of high-SECI conditions during 2014–2025: (a) number of years in which annual SECI exceeded the fixed P80 threshold of 0.912 and (b) persistent high-SECI areas. Persistent areas were defined as pixels exceeding this threshold in at least 8 of 12 years, with valid SECI observations in all 12 years

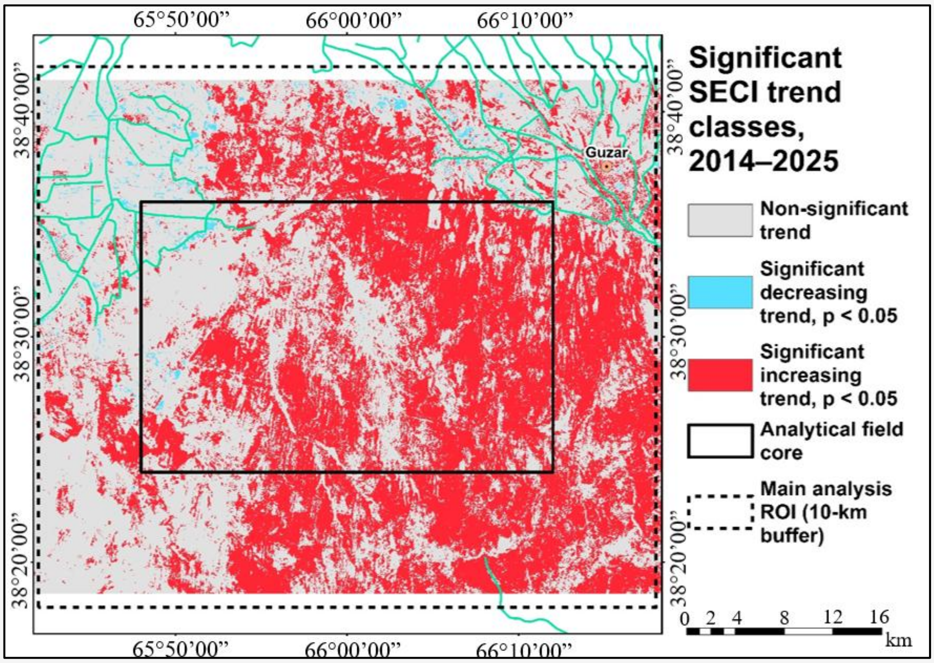

Figure 7: Significant SECI trend classes for 2014–2025 derived from Sen slope direction and the Mann–Kendall test. Non-significant pixels are shown in grey, while significant decreasing and increasing SECI trends are shown in blue and red, respectively ($p < 0.05$)

Table 4: Area of significant SECI trend classes by analysis zone

Zone	Increasing $p < 0.05$ km^2 (%)	Decreasing $p < 0.05$ km^2 (%)	Total significant $p < 0.05$ km^2 (%)	Total significant $p < 0.01$ km^2 (%)
Field core	399.9 (51.8%)	3.6 (0.46%)	403.5 (52.3%)	117.9 (15.3%)
ROI outside field core	615.5 (40.0%)	18.9 (1.23%)	634.4 (41.3%)	212.4 (13.8%)
Full 10-km ROI	1015.4 (44.0%)	22.5 (0.97%)	1037.9 (44.9%)	330.3(14.3%)

Table 5: Summary of SECI sensitivity and robustness tests

Sensitivity test	Scenario	Main result
Normalization	P1-P99	r=0.9997; agreement=97.1%; hotspot Jaccard=0.947
Normalization	P5-P95	r=0.9989; agreement=96.5%; hotspot Jaccard=0.841
ROI extent	5-25 km buffers	Mean SECI=0.686-0.803; mean Sen slope=0.00680-0.00715 SECI units/year
Leave-one-indicator-out	Without LST	r=0.985; agreement=57.2%; hotspot Jaccard=0.287
Leave-one-indicator-out	Without MSAVI	r=0.997; agreement=84.4%; hotspot Jaccard=0.655
Leave-one-indicator-out	Without BSI	r=0.999; agreement=83.2%; hotspot Jaccard=0.622

The full model uses LST, inverse MSAVI, and BSI with CRITIC weights. For leave-one-indicator-out tests, weights were recalculated with CRITIC

Using the stricter $p < 0.01$ threshold reduced the significant trend area, as expected, but did not change the overall direction of the result. Total significant trend area at $p < 0.01$ was 117.92 km2 (15.3%) in the field core and 212.37 km2 (13.8%) outside the field core within the 10-km ROI. This confirms that the increasing SECI tendency is not solely an artifact of the primary $p < 0.05$ threshold. The trend pattern should be interpreted as a monotonic increase in the relative SECI condition over parts of the study area. Because SECI is a composite of Landsat-derived thermal, vegetation, and bare-surface indicators, the trend does not isolate a single driving mechanism. The spatial overlap of increasing trends with both field-core and non-field dryland surfaces suggests that regional dryland surface dynamics, land-cover differences, and local surface modification may all contribute to the observed pattern.

3.4 Robustness, Sensitivity, and Interpretation Limits

Several sensitivity tests were used to evaluate whether the SECI results depended strongly on methodological choices (Table 5). Normalization sensitivity showed that the baseline P2-P98 normalization was stable relative to alternative percentile ranges. Compared with the baseline, P1-P99 normalization produced a correlation of 0.9997, class agreement of 97.1%, and persistent-hotspot Jaccard similarity of 0.947. P5-P95 normalization produced a correlation of 0.9989, class agreement of 96.5%, and Jaccard similarity of 0.841. These values indicate that the main spatial SECI pattern was not driven by a single normalization choice. The alternative ROI test showed that expanding the analysis buffer from 5 to 25 km reduced the mean SECI from 0.803 to 0.686 because progressively more surrounding dryland background was included. However, the mean Sen slope remained nearly stable, ranging only from 0.00715 to 0.00680 SECI units per year. This indicates that the trend result was less sensitive to ROI size than the absolute mean SECI value. The alternative 5, 15, 20, and 25 km buffers were therefore used only as sensitivity extents and were not treated as additional study zones.

The leave-one-indicator-out test further clarified the role of each component. Removing LST produced the largest change in class structure, with 57.2% class agreement and a persistent-hotspot Jaccard similarity of 0.287 relative to the full model. Removing MSAVI or BSI had smaller effects, with class agreements of 84.4% and 83.2%, respectively. This confirms that LST was the most influential component, consistent with its highest CRITIC weight. At the same time, high component correlations show that SECI primarily summarizes a common dryland surface gradient. SECI therefore provides a reproducible representation of relative surface environmental conditions, while additional data on infrastructure, production intensity, soil properties, land management, and climate variability would help explain the processes underlying the observed spatial and temporal patterns. The observed stability therefore applies only to the tested normalization, extent, and indicator scenarios and does not eliminate uncertainty associated with indicator redundancy or unmeasured environmental drivers.

4. Conclusions

This study applied a reproducible and sensitivity-tested Landsat-based framework for characterizing the spatial distribution and temporal dynamics of surface environmental conditions within and around the Shurtan gas field, Uzbekistan. Annual warm-season Landsat 8/9 composites for 2014–2025 were used to derive land-surface temperature, MSAVI, and BSI, which were integrated into the Surface Environmental Condition Index (SECI) using objective CRITIC weighting. The framework enabled consistent mapping of relative surface conditions, recurrent high-SECI areas, and long-term trends across the field core and the surrounding dryland landscape.

The results showed that the analytical field core had higher mean SECI values than the area outside the field core within the 10-km ROI. The field core was characterized by warmer surfaces, lower soil-adjusted vegetation signal, and stronger bare-surface expression. Mean SECI reached 0.863 in the field core, compared with 0.698 in the ROI outside the field core and 0.753 in the full 10-km ROI. Persistent high-SECI areas occupied 152.9 km², or 19.8% of the field core, compared with 10.2% in the area outside the field core. These results indicate that relatively high SECI conditions are more frequent and persistent within the field core, although they are not spatially exclusive to it. Land-cover stratification showed that high SECI values were mainly associated with dryland natural vegetation and bare or sparse surfaces, whereas cropland and built-up areas generally had lower SECI values. This confirms that SECI patterns in arid environments must be interpreted within land-cover context. High SECI values therefore represent recurrent combinations of thermal, vegetation, and bare-surface conditions within the arid landscape.

Trend analysis indicated that significant increasing SECI trends dominated during 2014–2025. At $p<0.05$, increasing trends covered 399.9 km², or 51.8% of the field core, while significant decreasing trends occupied only 3.6 km². The full 10-km ROI showed the same general tendency, with increasing trends covering 1015.4 km². The stricter $p < 0.01$ threshold reduced the significant trend area but did not change the dominant direction of change. This suggests a widespread monotonic increase in relative surface-condition intensity across parts of the study area. Sensitivity tests showed that the main SECI patterns were robust to alternative normalization ranges and analysis extents. The P1–P99 and P5–P95 normalization scenarios remained highly correlated with the baseline P2–P98 model, and the mean Sen slope was stable across 5–25 km analysis extents. The leave-one-indicator-out test confirmed that LST was the most influential component, while MSAVI and BSI provided additional information on vegetation response and bare-surface expression. These tests address only the evaluated normalization, spatial-extent, and indicator-selection scenarios and do not encompass uncertainty related to seasonal sampling, land-cover classification, residual atmospheric effects, unmeasured drivers, or the absence of direct field validation.

Compared with single-date assessments or subjectively weighted composite indices, the present framework provides several methodological advantages: objective CRITIC weighting that accounts for indicator contrast and redundancy, fixed normalization that preserves temporal comparability, explicit evaluation of high-SECI persistence and trend significance, and sensitivity testing of normalization, spatial extent, and indicator selection. These features improve the reproducibility, temporal consistency, and interpretive transparency of the assessment. However, because no direct benchmark comparison with all alternative methods was performed, these advantages should not be interpreted as evidence of universal methodological superiority. Furthermore, the framework characterizes observable surface environmental conditions and does not establish causal attribution.

The principal limitations are the absence of direct field validation and spatially explicit production and infrastructure histories, the restriction to warm-season observations, the possibility of residual atmospheric effects, and the potential confounding influence of natural aridity and land-cover differences. Accordingly, SECI should be treated as a screening baseline rather than as direct evidence of environmental impact or gas-production effects. Overall, the applied framework provides a conservative baseline for mapping and interpreting surface environmental conditions in arid hydrocarbon landscapes with limited auxiliary data. Its main value lies in identifying spatially persistent and temporally increasing surface-condition patterns that can guide further investigation and help identify candidate areas for targeted field surveys and monitoring. However, SECI does not identify the drivers of these patterns.

More broadly, long-term, openly available Landsat observations combined with objective weighting and explicit sensitivity testing can provide a transparent screening baseline for data-limited arid industrial regions. For environmental monitoring, the resulting products can help identify candidate areas for field surveys and guide the design or densification of monitoring networks. For policy and environmental management, they may support the prioritization of field verification and additional data collection, but they should not be used as stand-alone evidence of environmental impact or regulatory non-compliance. For the scientific community, the workflow provides a reproducible framework that can be tested and adapted in other arid industrial landscapes, subject to local recalibration and field validation. Future work should integrate production records, infrastructure-development histories, vegetation and soil surveys, in-situ surface-temperature and moisture measurements, climate variability, and deformation observations to distinguish natural dryland dynamics from local surface modification and possible production-related effects.

Acknowledgements

This work was supported by State Basic funding from the Academy of Sciences of the Republic of Uzbekistan. Figures were prepared using the ArcGIS ver.10.8 graphic package.

References

[1] Safriel, U., Adeel, Z., Niemeijer, D., Puigdefabregas, J., White, R., Lal, R., Winslow, M., Ziedler, J., Prince, S., Archer, E. and King, C., (2005). Dryland Systems. In: Hassan, R., Scholes, R. and Ash, N. (Eds.), *Ecosystems and Human Well-Being: Current State and Trends*, Vol. 1; 623-662. Island Press, Washington, DC. [Online]. Available: https://www.millenniumassessment.org/documents/document.291.aspx.pdf. [Accessed: Jul. 12, 2026].

[2] Dubovyk, O., (2017). The Role of Remote Sensing in Land Degradation Assessments: Opportunities and Challenges. *European Journal of Remote Sensing*, Vol. 50(1); 601-613. https://doi.org/10.1080/22797254.2017.1378926.

[3] Higginbottom, T. P. and Symeonakis, E., (2014). Assessing Land Degradation and Desertification Using Vegetation Index Data: Current Frameworks and Future Directions. *Remote Sensing*, Vol. 6(10); 9552-9575. https://doi.org/10.3390/rs6109552.

[4] Wessels, K. J., Prince, S. D., Malherbe, J., Small, J., Frost, P. E. and Van Zyl, D., (2007). Can Human-Induced Land Degradation Be Distinguished from the Effects of Rainfall Variability? A Case Study in South Africa. *Journal of Arid Environments*, Vol. 68(2); 271-297. https://doi.org/10.1016/j.jaridenv.2006.05.015.

[5] Veron, S. R., Paruelo, J. M. and Oesterheld, M., (2006). Assessing Desertification. *Journal of Arid Environments*, Vol. 66(4); 751-763. https://doi.org/10.1016/j.jaridenv.2006.01.021.

[6] Allred, B. W., Smith, W. K., Twidwell, D., Haggerty, J. H., Running, S. W., Naugle, D. E. and Fuhlendorf, S. D., (2015). Ecosystem Services Lost to Oil and Gas in North America. *Science*, Vol. 348(6233); 401-402. https://doi.org/10.1126/science.aaa4785.

[7] Wang, H., (2021). The Impact of Shale Oil and Gas Development on Rangelands in the Permian Basin Region: An Assessment Using High-Resolution Remote Sensing Data. *Remote Sensing*, Vol. 13(4). https://doi.org/10.3390/rs13040824.

[8] Finn, S. P. and Knick, S. T., (2011). Changes to the Wyoming Basins Landscape from Oil and Natural Gas Development. *Sagebrush Ecosystem Conservation and Management: Ecoregional Assessment Tools and Models for the Wyoming Basins*; 69-87. Allen Press. [Online]. Available: https://www.usgs.gov/publications/chapter-3-changes-wyo ming-basins-landscape-oil-and-natural-gas-development. [Accessed: Jul. 12, 2026].

[9] Tyree, G. L., Chappell, A., Villarreal, M. L., Dhital, S., Duniway, M. C., Edwards, B. L., Faist, A. M., Nauman, T. W. and Webb, N. P., (2024). Oil and Gas Development Influences Potential for Dust Emission from the Upper Colorado River Basin, USA. *Earth Surface Processes and Landforms*, Vol. 49(11); 3292-3307. https://doi.org/10.1002/esp.5887.

[10] Jones, I. L., Bull, J. W., Suttle, K. B., Esipov, A. V. and Milner-Gulland, E. J., (2014). Quantifying Habitat Impacts of Natural Gas Infrastructure to Facilitate Biodiversity Offsetting. *Ecology and Evolution*, Vol. 4(1); 79-90. https://doi.org/10.1002/ece3.884.

[11] Couloigner, I., Fallah, B., Hanes, A., Mirzaei, M., Dempsey, D., and Bertazzon, S. (2024). Multiscale Space-Time Analysis of Environmental Changes in the Oil Sands Area (Alberta, Canada). *International Journal of*

Geoinformatics, Vol. 20(4), 56–73. https://doi.org/10.52939/ijg.v20i4.3151.

[12] Gao, C., Ren, X., Fan, L., He, H., Zhang, L., Zhang, X., Li, Y., Zeng, N. and Chen, X., (2023). Assessing the Vegetation Dynamics and Its Influencing Factors in Central Asia from 2001 to 2020. *Remote Sensing*, Vol. 15(19); 4670. https://doi.org/10.3390/rs15194670.

[13] Ulmishek, G. F., (2004). *Petroleum Geology and Resources of the Amu-Darya Basin: Turkmenistan, Uzbekistan, Afghanistan, and Iran*. U.S. Geological Survey Bulletin 2201-H. https://doi.org/10.3133/b2201H.

[14] Fazilova, D., Tukhtameshov, F., Rakhimberdieva, M., Kazakov, A. and Magdiev, K., (2025). GNSS-Based Subsidence Monitoring of Shurtan's Gas Reservoir in Uzbekistan. *Acta IMEKO*, Vol. 14(1); 1-6. https://doi.org/10.21014/actaimeko.v14i1.1866

[15] Sims, N. C., Newnham, G. J., England, J. R., Guerschman, J., Cox, S. J. D., Roxburgh, S. H., Viscarra Rossel, R. A., Fritz, S. and Wheeler, I., (2021). *Good Practice Guidance for SDG Indicator 15.3.1: Proportion of Land That Is Degraded over Total Land Area, Version 2.0*. United Nations Convention to Combat Desertification (UNCCD), Bonn, Germany. [Online]. Available: https://www.unccd.int/sites/default/files/documents/2021-09/UNCCD_GPG_SDG-Indicator15.3.1_version2_2021.pdf. [Accessed: Jul. 12, 2026].

[16] Hu, X. and Xu, H., (2018). A New Remote Sensing Index for Assessing the Spatial Heterogeneity in Urban Ecological Quality: A Case from Fuzhou City, China. *Ecological Indicators*, Vol. 89; 11-21. https://doi.org/10.1016/j.ecolind.2018.02.006.

[17] Xu, H., Wang, Y., Guan, H., Shi, T. and Hu, X., (2019). Detecting Ecological Changes with a Remote Sensing-Based Ecological Index (RSEI) Produced Time Series and Change Vector Analysis. *Remote Sensing*, Vol. 11(20); 2345. https://doi.org/10.3390/rs11202345.

[18] Sun, C., Li, J., Wang, C. and Li, J., (2022). Ecological Quality Assessment and Monitoring Using a Time-Series Remote Sensing Ecological Index. *GIScience & Remote Sensing*, Vol. 59(1); 1793-1816. https://doi.org/10.1080/15481603.2022.2138010.

[19] Zheng, Z., Wu, Z., Chen, Y., Yang, Z. and Marinello, F., (2022). Instability of Remote Sensing-Based Ecological Index (RSEI) and Its Improvement for Time Series Analysis. *Science of the Total Environment*, Vol. 814; 152595. https://doi.org/10.1016/j.scitotenv.2021.152595.

[20] Malczewski, J., (2000). On the Use of Weighted Linear Combination Method in GIS: Common and Best Practice Approaches. *Transactions in GIS*, Vol. 4(1); 5-22. https://doi.org/10.1111/1467-9671.00035.

[21] Yadav, B., Malav, L. C., Jimenez-Ballesta, R., Kumawat, C., Patra, A., Patel, A., Jangir, A., Nogiya, M., Meena, R. L., Moharana, P. C., Kumar, N., Sharma, R. P., Yadav, L. R., Obi Reddy, G. P. and Mina, B. L., (2023). Modeling and Assessment of Land Degradation Vulnerability in Arid Ecosystem of Rajasthan Using Analytical Hierarchy Process and Geospatial Techniques. *Land*, Vol. 12(1). https://doi.org/10.3390/land12010106.

[22] Thammaboribal, P., Triapthti, N., and Lipiloet, S. (2025). Using of Analytical Hierarchy Process (AHP) in Disaster Management: A Review of Flooding and Landslide Susceptibility Mapping. *International Journal of Geoinformatics*, Vol. 21(4), 177–196. https://doi.org/10.52939/ijg.v21i4.4091.

[23] Saaty, T. L., (1980). *The Analytic Hierarchy Process: Planning, Priority Setting, Resource Allocation*. McGraw-Hill, New York.

[24] Shannon, C. E., (1948). A Mathematical Theory of Communication. *Bell System Technical Journal*, Vol. 27(3); 379-423. https://doi.org/10.1002/j.1538-7305.1948.tb01 338.x.

[25] Zeleny, M., (1982). *Multiple Criteria Decision Making*. McGraw-Hill, New York.

[26] Diakoulaki, D., Mavrotas, G. and Papayannakis, L., (1995). Determining Objective Weights in Multiple Criteria Problems: The CRITIC Method. *Computers & Operations Research*, Vol. 22(7); 763-770. https://doi.org/10.1016/0305-0548(94)00059-H.

[27] Berdyyev, A., Ayek, A. M., Hasan, F. and Kurbanov, S., (2024). Desertification Monitoring using Machine Learning Techniques with Multiple Indicators Derived from Sentinel-2 in Turkmenistan. *Remote Sensing*, Vol. 16(23). https://doi.org/10.3390/rs16234525.

[28] Yang, C., Zhang, D., Zhao, C., Han, B., Sun, R., Du, J. and Chen, L., (2019). Ground Deformation Revealed by Sentinel-1 MSBAS-InSAR Time-Series over Karamay Oilfield, China. *Remote Sensing*, Vol. 11(17). https://doi.org/10.3390/rs11172027.

[29] Bayramov, E., Buchroithner, M. F., Kada, M. and Zhunusbayev, A., (2022). Multi-Temporal SAR Interferometry for Vertical Displacement Monitoring over the Tengiz Oilfield, Kazakhstan. *Frontiers in Environmental*

ISSN: 1686-6576 (Printed) | ISSN 2673-0014 (Online) |

Science, Vol. 10; 783351. https://doi.org/10.3389/fenvs.2022.783351.

[30] Yu, Y., Yin, J., Zheng, J., Li, F., Tao, C., Xu, X. and Wu, H., (2015). Division and Resources Evaluation of Hydrocarbon Plays in the Amu Darya Basin, Central Asia. *Petroleum Exploration and Development*, Vol. 42(6); 819-826. https://doi.org/10.1016/S1876-3804(15)30078-1.

[31] Hosseinyar, G., Moussavi-Harami, R., Abdollahie Fard, I., Mahboubi, A. and Noemani Rad, R., (2019). Seismic Geomorphology and Stratigraphic Trap Analyses of the Lower Cretaceous Siliciclastic Reservoir in the Kopeh Dagh-Amu Darya Basin. *Petroleum Science*, Vol. 16(4); 776-793. https://doi.org/10.1007/s12182-019-0347-1.

[32] Padmanaban, R., Bhowmik, A. K. and Cabral, P., (2017). A Remote Sensing Approach to Environmental Monitoring in a Reclaimed Mine Area. *ISPRS International Journal of Geo-Information*, Vol. 6(12). https://doi.org/10.3390/ijgi6120401.

[33] Bayramov, E., Buchroithner, M. F. and Kada, M., (2020). Radar Remote Sensing to Supplement Pipeline Surveillance Programs through Measurements of Surface Deformations and Identification of Geohazard Risks. *Remote Sensing*, Vol. 12(23). https://doi.org/10.3390/rs12233934.

[34] Zanaga, D., Van De Kerchove, R., Daems, D., De Keersmaecker, W., Brockmann, C., Kirches, G., Wevers, J., Cartus, O., Santoro, M., Fritz, S., Lesiv, M., Herold, M., Tsendbazar, N. E., Xu, P., Ramoino, F. and Arino, O., (2022). *ESA WorldCover 10m 2021 v200*. Zenodo, https://doi.org/10.5281/zenodo.7254221.

[35] U.S. Geological Survey, (2024). *Landsat 8-9 Collection 2 Level-2 Science Product Guide, LSDS-1619, Version 6.0*. U.S. Geological Survey. [Online]. Available: https://www.usgs.gov/media/files/landsat-8-9-collection-2-level-2-science-product-guide. [Accessed: Jul. 12, 2026].

[36] Gorelick, N., Hancher, M., Dixon, M., Ilyushchenko, S., Thau, D. and Moore, R., (2017). Google Earth Engine: Planetary-Scale Geospatial Analysis for Everyone. *Remote Sensing of Environment*, Vol. 202; 18-27. https://doi.org/10.1016/j.rse.2017.06.031.

[37] U.S. Geological Survey, (2024). How Do I Use a Scale Factor with Landsat Level-2 Science Products? *USGS Landsat Missions*. [Online]. Available: https://www.usgs.gov/faqs/how-do-i-use-scale-factor-landsat-level-2-science-products. [Accessed: Jul. 12, 2026].

[38] Thammaboribal, P., (2024). Investigating Land Surface Temperature Variation and Land Use Land Cover Changes in Pathumthani, Thailand (1997-2023) Using Landsat Satellite Imagery: A Comprehensive Analysis of LST and Urban Hot Spots (UHS). *International Journal of Geoinformatics*, Vol. 20(2); 27-41. https://doi.org/10.52939/ijg.v20i2.3063.

[39] Qi, J., Chehbouni, A., Huete, A. R., Kerr, Y. H. and Sorooshian, S., (1994). A Modified Soil Adjusted Vegetation Index. *Remote Sensing of Environment*, Vol. 48(2); 119-126. https://doi.org/10.1016/0034-4257(94)90134-1.

[40] Rikimaru, A., Roy, P. S. and Miyatake, S., (2002). Tropical Forest Cover Density Mapping. *Tropical Ecology*, Vol. 43(1); 39-47.

[41] Sen, P. K., (1968). Estimates of the Regression Coefficient Based on Kendall's Tau. *Journal of the American Statistical Association*, Vol. 63(324); 1379-1389. https://doi.org/10.1080/01621459.1968.10480934.

[42] Mann, H. B., (1945). Nonparametric Tests against Trend. *Econometrica*, Vol. 13(3); 245-259. https://doi.org/10.2307/1907187.

[43] Kendall, M. G., (1975). *Rank Correlation Methods*, 4th ed. Charles Griffin, London.